





Enhanced thermoelectric properties of $(\text{SnS})_{1-x}(\text{SnO})_x$: $x \leq 10.79\%$ nanocomposites prepared by polyol method

Chanderbhan Chotia¹ , Tarachand¹, Gunadhori Singh Okram^{1,*} , Yung-Kang Kuo², and Shamima Hussain³

¹UGC – DAE Consortium for Scientific Research, University Campus, Khandwa Road, Indore 452001, India

²Department of Physics, National Dong Hwa University, Hualien 97401, Taiwan

³UGC – DAE Consortium for Scientific Research, Kalpakkam Node, Via Kokilamedu Gate, Kokilamedu, TN 603104, India

Received: 26 October 2020

Accepted: 8 March 2021

Published online:

24 March 2021

© The Author(s), under exclusive licence to Springer Science+Business Media, LLC, part of Springer Nature 2021

ABSTRACT

$(\text{SnS})_{1-x}(\text{SnO})_x$: $x = 0, 3.57\%, 7.16\%$, and 10.79% nanocomposites (NCs) have been successfully synthesized using a simple polyol method. XRD data analysis shows formation of SnS and SnO NCs with an average crystallite size in the range from 30 to 35 nm. The Rietveld refinement analysis indicates layered orthorhombic crystal structure. FESEM images display the morphology of nanoflakes and nanoplates. Their positive Seebeck coefficients (α) suggest the p-type conduction. This is consistent with the deficiency of Sn found. $(\text{SnS})_{0.9284}(\text{SnO})_{0.0716}$ NC exhibits a thermal conductivity (κ) of $0.75 \text{ Wm}^{-1} \text{ K}^{-1}$ at 300 K. Electrical (σ) and thermal conductivities are decreased, but α enhances with increasing x . Consequently, the dimensionless figure of merit (ZT) increases with increasing x up to 7.16% for which ZT at 325 K is 0.0036. This is 55% enhancement compared to the pure SnS that opens a new window for improvement of thermoelectric performance near room temperature.

1 Introduction

In order to reduce the fossil fuel consumptions and meet global energy demand, thermoelectric (TE) devices have been emerged as potential candidates which use the waste heat to produce electricity without emitting harmful gases or noise with good sustainability [1, 2]. Therefore, they are considered to be a solution to energy crisis and environmental problems of the world [3]. To fulfill this aim, a TE material should require large Seebeck coefficient α

and electrical conductivity σ , but low thermal conductivity due to electrons κ_e and phonons κ_l so that the dimensionless figure of merit $ZT = \frac{\alpha^2 \sigma}{\kappa_e + \kappa_l} T$ is maximum, where T is absolute temperature [4]. However, their interdependence is a serious issue in the usual materials to obtain large ZT [2]. This is circumvented through the introduction of a second phase [5], nanocomposites [6, 7], nanostructures [8, 9], low sound velocity [10], alloy defects [11], liquid phonons [12], lattice anharmonicity [13], solid solution [14], and band modification [15–17]. In

Address correspondence to E-mail: okram@csr.res.in; okramgs@gmail.com

addition to their operational advantages for TE devices, the materials must be cheap, nontoxic, long lasting, and abundant [18]. Among various potential materials such as SnSe [3, 19], SnTe [20, 21], SnS [22–24], $\text{Si}_{1-x}\text{Ge}_x$ [25], $\text{Mg}_2\text{Si}_{1-x}\text{Sn}_x$ [26], Ag_9GaSe_6 [27] and half-Heusler [28], tin monosulfide/oxide (SnS/SnO) is increasingly being investigated as a TE material because it is neither scarce nor expensive [29]. Moreover, SnS is used widespread in lithium-ion batteries, solar cells, near-infrared detectors, photoconductors, optoelectronics, photoluminescence, sensors, photovoltaic materials, micro-batteries, spintronics, capacitors, and storage devices [30, 31].

In this direction, the semiconducting and nontoxic layered SnS with indirect band gap of 1.1–1.5 eV, as a family of TE materials Sn(Te/Se) [2, 18–20], attracts special attention due to its very high α/κ and moderate σ [14, 22, 32–36]. At room temperature, it crystallizes into an orthorhombic crystal structure with space group Pnma having double layers of covalently bonded alternating S and Sn atoms. The two adjacent layers bond loosely via van der Waals forces, which make them suitable for TE applications. As Parker et al. predicted using band structure calculation, p-type layered SnS can have high α with very low κ and its TE performance can be enhanced by increasing σ through appropriate doping [33]. Furthermore, an increased ZT value of 0.6 (923 K) and 0.65 (850 K) was reported in polycrystalline SnS on doping Ag and Na with hole concentrations (n_p) of 2.7 and $20 \times 10^{18} \text{ cm}^{-3}$, respectively [32, 34]. Increased n_p and mobility in Na-doped single-crystalline SnS have led to a ZT value of 1.0–1.1 at 873 K [35, 36]. These high ZT values show the promising nature of this 2D SnS compound for TE applications.

The ZT improvement through reduced κ in the design of chalcogenide nanocomposites covered with an oxide layer attracts particular attention, as they not only allow a partial decoupling of κ and σ , but also increase the stability of the host. Kim et al. [37] reported a high ZT ~ 1.5 at 329–360 K for ZnO-coated- $\text{Bi}_{0.4}\text{Sb}_{1.6}\text{Te}_3$ due to strong scattering of phonons and enhanced electronic carrier density through impurity doping at the heterogeneous grain boundaries. Also, the TE performance of oxide materials can be enhanced through their NCs [38]. Abundant and nontoxic SnO [39] with positive α has, thus, been emerged as a potential candidate for TE material [39–41]. Therefore, we prepared Te-free Sn-deficient

SnS via a simple polyol method and introduced SnO to improve TE performance near room temperature. These well-characterized $(\text{SnS})_{1-x}(\text{SnO})_x$ nanocomposites show a significant reduction in thermal conductivity with enhanced α as the SnO content increases and hence a significantly improved ZT at 325 K.

2 Experimental section

2.1 Synthesis

2.1.1 Synthesis of SnS

Tin sulfide nanoparticles (NPs) have successfully been synthesized in our laboratory using a simple polyol method [42]. We used 4 mmol (millimole) SnCl_2 (99%, Alfa) and 4.1 mmol of thiourea (99%, Alfa) as Sn and S sources, respectively. They were dissolved in 50 ml of diethylene glycol (DEG) in a three-neck flask in Ar atmosphere. This solution was heated at a constant rate of $25 \text{ }^\circ\text{C min}^{-1}$ to $200 \text{ }^\circ\text{C}$ at which the color of the solution was changed from gray to black. It was maintained for 2 h at $220 \text{ }^\circ\text{C}$ to complete the reaction. Then the solution was kept to cool naturally to room temperature. The precipitate (ppt) was removed from the suspension by centrifugation at 12,000 rpm for 12 min and decantation. The ppt was then dispersed in ethanol and subjected to probe ultrasonicator for 5 min for uniform dispersion. The dispersed ppt was then centrifuged for a further 4 min at the same rpm and the ethanol was decanted. The ppt was redispersed in ethanol and these purification steps were repeated three times. Finally, the ethanol was discarded and black ppt of NPs was dried at $60 \text{ }^\circ\text{C}$ for 1 h in vacuum oven. The powder, thus, obtained was used for various characterizations and further investigations and marked as SS0.

2.1.2 Synthesis of $(\text{SnS})_{1-x}(\text{SnO})_x$: $x = 3.57\%$, 7.16% , and 10.79% nanocomposites

For introduction of SnO in SnS, additional 0.2, 0.4, and 0.6 mmol SnCl_2 in each was added separately for $x = 5, 10,$ and 15% SnCl_2 samples, respectively, in the naturally cooled solutions below $80 \text{ }^\circ\text{C}$ just after the completion of reaction at $220 \text{ }^\circ\text{C}$ for 2 h of the identically prepared SS0 sample batches. Then, the

solutions were heated independently at $6\text{ }^{\circ}\text{C min}^{-1}$ to reach $220\text{ }^{\circ}\text{C}$, which were maintained for another 2 h. After this, washing steps, similar to SS0, were performed for each sample. These $x = 5, 10,$ and 15% SnCl_2 samples, therefore, stand out to be nominally $(\text{SnS})_{1-x}(\text{SnO})_x$: $x = 3.57\%, 7.16\%,$ and 10.79% considering that the stoichiometric SnS and SnO are formed. They were coded as SS5, SS10, and SS15. Resulting NPs were consolidated into rectangular pellets of $8\text{ mm} \times 4\text{ mm} \times 2\text{ mm}$ size under a uniaxial pressure of $\sim 1.1\text{ GPa}$ and followed by an annealing process at $300\text{ }^{\circ}\text{C}$ for 5 h under a continuous flow of Ar gas in a tubular furnace.

2.2 Characterization

The formation of a crystalline phase was characterized using X-ray diffraction (XRD), which was collected using a Bruker D8 Advance X-ray diffractometer with Cu K_{α} radiation (1.54 \AA) in the angular range (2θ) from 20° to 80° with a scanning angle step size of 0.02° , 0.5 s wait time, and nearly $4 \times 10\text{ mm}^2$ slit width. The energy dispersive analysis of X-ray (EDAX) measurements were done to analyze elemental composition and the particle size distribution was examined using a field emission scanning electron microscopic (FESEM) images using Carl Zeiss AURIGA FIBSEM in the secondary emission mode. The Seebeck coefficient (α) was measured by load-based home-made setup by mounting the annealed pellets between the flat ends of two oxygen-free highly conductive cylindrical copper blocks [43]. The electrical conductivity using guarded two-probe and four-point probe methods [44] was measured in the temperature range of $160\text{--}325\text{ K}$ in a specially developed commercial Dewar; measurements had $\pm 3\%$ error. Thermal conductivity (κ) was measured using a heat pulse technique in the temperature range $5\text{--}330\text{ K}$ [45].

3 Results and discussion

3.1 X-ray diffraction (XRD) study

The powder XRD patterns of all the samples are shown in Fig. 1a. All the diffraction peaks in SS0 agree well with the standard JCPDS card No. 00-039-0354 that confirms the formation of single-phase polycrystalline SnS NPs with orthorhombic crystal

structure. However, there are extra peaks at 28.9° and 49.9° in SS5, SS10, and SS15. They correspond to SnO phase with orthorhombic crystal structure that agrees with the literature [46]. Values of lattice parameters $a = 4.32\text{ \AA}$, $b = 11.19\text{ \AA}$, and $c = 3.98\text{ nm \AA}$ for SnS, and $a = 5.0\text{ \AA}$, $b = 5.74\text{ \AA}$, and $c = 11.04\text{ \AA}$ for SnO from the literature [46, 47] were used initially in the Rietveld refinement. This is to confirm the single-phase nature of SS0, and dual-phase nature of SS5, SS10, and SS15 (Figs. 1b, c and S1a,b); various parameters are tabulated in Table 1. With increasing x , there is no systematic change of the lattice parameters, the volume, the mass density, and the Scherrer size. The lattice parameters and the volume of the unit cell of SnS in the present case are higher than those in Skelton [48] and a higher density than other reports [14, 23, 34, 49, 50]. The mass density of the SnO phase found is comparable to earlier report [46]. The fraction of SnO found from the Rietveld fitting is $3.57\%, 7.16\%,$ and 10.79% as against the nominal $6.66\%, 12.50\%,$ and 17.63% in SS5, SS10, and SS15, respectively. They may indicate an incomplete formation of SnO or an incomplete reduction of SnCl_2 . The crystallite size of these samples was studied using full-width at half maximums (FWHMs) of the XRD peaks in the Scherrer's formula. We chose 5–6 peaks to calculate the average crystallite sizes. The calculated values of average crystallite size for SnS phase are $30.5 \pm 0.6\text{ nm}$, $33.5 \pm 0.7\text{ nm}$, $39.1 \pm 0.8\text{ nm}$, and $25.6 \pm 0.5\text{ nm}$ in SS0, SS5, SS10, and SS15, respectively (Fig. 1d, bottom inset). They are $22.9 \pm 0.4\text{ nm}$, $30.1 \pm 0.6\text{ nm}$, and $27.3 \pm 0.5\text{ nm}$ in SS5, SS10, and SS15, respectively, for SnO phase; for this chemical phase, the average crystallite size of two peaks' FWHM results was used. Among all these samples, SS10 has the lowest unit cell volume, highest crystallite size, and highest mass density (Fig. 1d, top inset) of the SnS phase (Fig. 1d and Table 1).

The layered structure was generated for all samples using the VESTA CIF file after the Rietveld refinement (Fig. 1e as a typical example). The orthorhombic crystal structure of SnS has an armchair along the b -axis and a zigzag along the c -axis. The L1 and L2 denote the bond lengths for out of plane and in-plane, respectively, of the optimized atomic structures of AB-stacked multi-layer SnS structure (Fig. 1e). The calculated values of L1 and L2, and the interlayer spacing (d) for AB-stacked SnS bilayers, are given in Table 2 and shown in Fig. 1f. The value of L2 is greater than the value of L1 in all

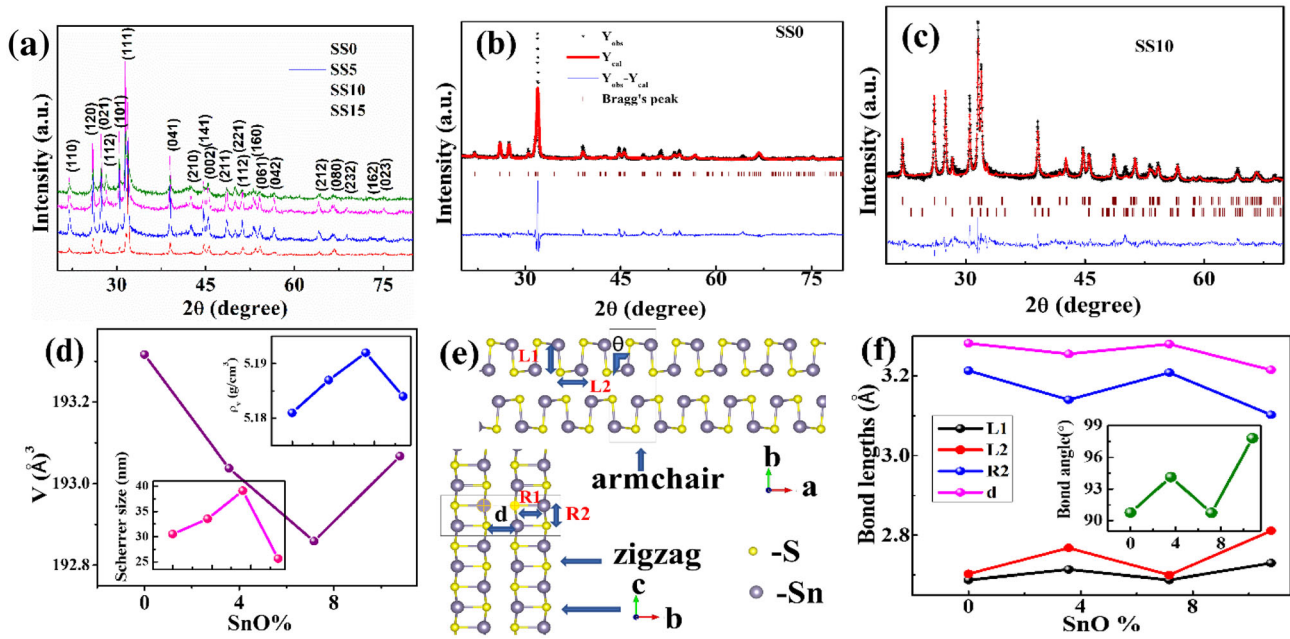


Fig. 1 a XRD patterns of SS0, SS5, SS10, and SS15. Rietveld refinement of b SS0 and c SS10. d Unit cell volume of SnS phase, V , versus SnO%. e Layered crystal structure of single-phase SnS. f Bond lengths of SnS phase versus SnO%, symbols used in e are

used here. Insets: d, bottom, Scherrer size versus SnO%, and top, mass density versus SnO%; f bond angles versus SnO% are indicated

Table 1 Lattice parameters, unit cell volume, mass density (ρ_v), Scherrer size, χ^2 , and phase fraction of the samples

Samples	Phase	Lattice parameter			Volume (\AA^3)	ρ_v (g cm^{-3})	Scherrer size (nm)	Fraction (%)
		a (\AA)	b (\AA)	c (\AA)				
SS0	SnS	4.325 (4.251	11.204 (11.082	3.989 (3.978	193.317 (187.4	5.181	30.5	100
		[49])	[49])	[49])				
SS5	SnS	4.317	11.205	3.989	193.038	5.187	33.5	96.43
	SnO	5.104	5.859	10.975	328.301	5.472	22.9	3.57
SS10	SnS	4.320	11.197	3.986	192.859	5.192	39.1	92.84
	SnO	5.106	5.861	10.972	328.431	5.448	30.1	7.16
SS15	SnS	4.317	11.202	3.991	193.068	5.184	25.6	89.21
	SnO	4.116	5.861	10.997	329.650	5.425	27.3	10.79

samples (Fig. 1e and Table 2). Park et al. reported the bond lengths L1 and L2 for double-layered SnS as 2.56 and 2.70 Å, respectively [51]. Xin et al. reported L1 = 2.66 and L2 = 2.68 Å, respectively, for bulk SnS [52], but these bond lengths are slightly longer than these reports [51, 52] in the present work. This may indicate perhaps the lattice expansion in NPs compared to that of bulk. In the family of 2D materials, the low-temperature phase of SnS crystallizes in an orthorhombic structure made up of covalently bonded double layers of alternating Sn and S atoms, while the neighboring layers are connected by long-

range electrostatic forces [53, 54]. The interlayer distance is slightly longer than 3.2 Å (Fig. 1f and Table 2), which corresponds to the equilibrium distance of ~ 3.4 Å via van der Waals interaction [55]. Each unit cell consists of two SnS layers and one of the long-distance S resides on the neighboring SnS layer. This weak Sn–S interaction binds two SnS layers together to form a bilayer structure that is perpendicular to the b -axis with Sn and S atoms covalently bonded within the layers and weak van der Waals bonds hold the layers. The van der Waals interaction between the double layers results in a

Table 2 Bond lengths and bond angles in SnS phase as indicated in Fig. 1e, f armchair and zigzag structure of the samples

Samples	Bond lengths (Å)					Bond angle (degree)
	L1	L2	R1	R2	<i>d</i>	
SS0	2.688	2.703	2.688	3.213	3.282	90.75
SS5	2.714	2.768	2.714	3.140	3.255	94.13
SS10	2.688	2.700	2.700	3.208	3.280	90.73
SS15	2.730	2.811	2.730	3.102	3.215	97.80

chemically inert surface with few surface states. This fault-tolerant surface reduces the loss of carrier recombination due to defects at the grain boundaries [56].

The bond length (R1) along the *b*-axis in zigzag structure is the (nearly) same as L1, but the bond length (R2) along *c*-axis in zigzag structure is larger than R1, L1, and L2 (Fig. 1e and Table 2). This means that the bond along the *c*-axis is weaker than along the *a*-axis. The length R2 is comparable and somewhat smaller than the interlayer spacing *d*. The bond angle is for S1–Sn1–S1 bond and is the largest in SS15. In addition, while L1 and L2 are the largest, R2 and *d* are the smallest in SS15. These bond lengths are comparable to the bulk SnS [57]. Due to its layered structure, SnS also shows strong anisotropic vibrational properties, which are important for thermal conductivity in order to optimize the ZT.

3.2 FESEM and EDAX study

The microstructure of the samples was examined using representative FESEM images of SS0 and SS5 (Fig. 2a, b). As can be seen, the NPs are of a relatively uneven size with different thicknesses and shapes. SS0 shows a fern-like arrangement of smaller particles together with much larger leaf-like nanosheets or nanoflakes. Their average thickness is about 25 nm, average width of 60 nm, and the length varies between 90 and 500 nm (Fig. 2a). The crystallite size is larger than the average thickness, but smaller than the average width and average length of the SS0 NPs. This is attributed to relatively much smaller number of sheets than that of dominant majority of larger ones. The average thickness of SS5 around 65 nm (Fig. 2b) is larger than the average crystallite size associated with radical diminution of the fern-like smaller particles, nanosheets, or nanoflakes. The disappearance of the latter is indicative of the enhanced grain growth of SnS sheets (Figs. 2a and

2b) into relatively uniform thicker sheets with the probable formation of NCs.

The atomic percentage of the constituent elements is determined from EDAX data for pure SnS (SS0), illustrated in Fig. 2c, wherein point of interest in its FESEM image is indicated (inset). This ruled out the presence of any impurity elements in SS0 with 52.91 at.% of S and 47.09 at.% of Sn. When we consider the formation of stoichiometric SnS, it is 5.82% Sn-deficient (or S-rich) and in well accordance with earlier reports [58, 59] in which they observed Sn vacancy in SnS and a hole-dominant conduction [59]. The presence of O is evident from the EDAX data of SS5–SS15 (Fig. 2d–f). The percentage ratios of constituent elements Sn:S:O are 40.57:50.2:9.23 in SS5, 35.81:47.38:16.81 in SS10, and 35.29:43.97:20.73 in SS15. It is to note that even when Sn content is increased in the reactions in SS5–SS15, there is still a deficiency of Sn. This means that there is always a p-type conduction. Here, the percentage of O is higher than that found in the Rietveld refinement. It is attributed to the reaction by-product due to the polyol method in which the metal hydroxide is present on the surface.

4 Electrical transport study

The electrical conductivity (σ) for all samples increases nearly exponentially with increasing temperature, which indicates their semiconducting behavior (Fig. 3a). It is 7.25 times larger for pure SS0 than that of SS15 at 300 K or larger than that of bulk SnS [14, 34, 49]. The introduction of an additional resistive component of SnO leads to a systematic reduction of σ with increasing *x*. This confirms that more resistive SnO coats or blocks more conductive surface of SnS NPs. In addition to these features, close observations show faster drops in the electrical conductivity below 183, 185, 196, and 200 K for *x* = 0, 3.57%, 7.16%, and 10.79%. They suggest in general

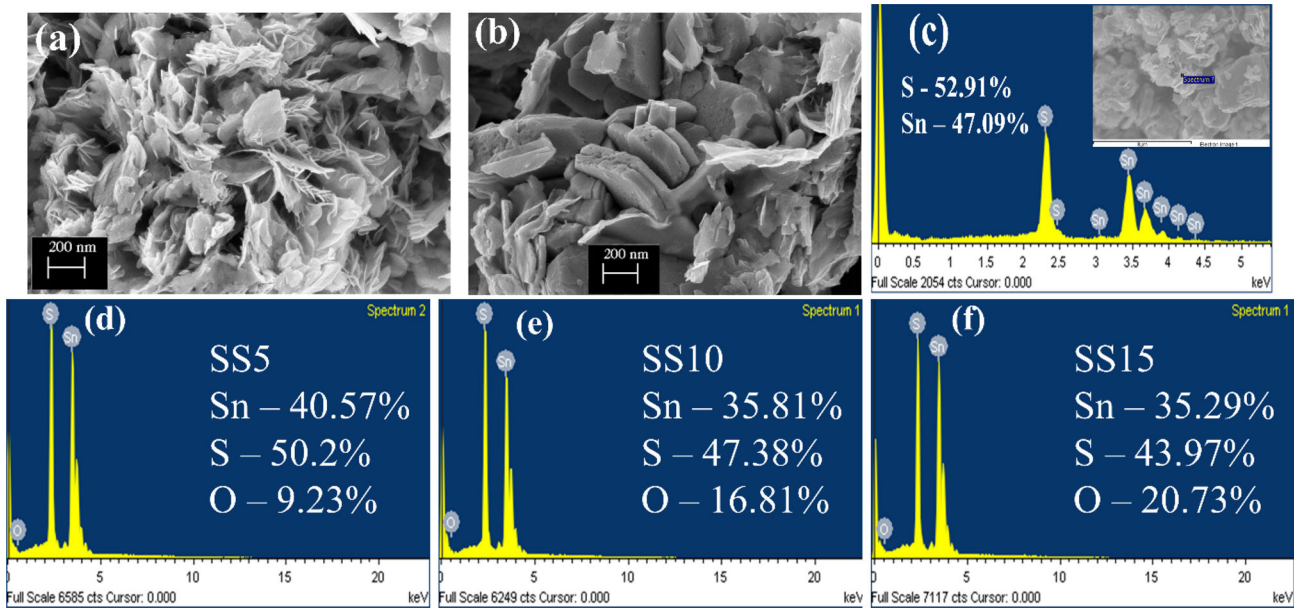
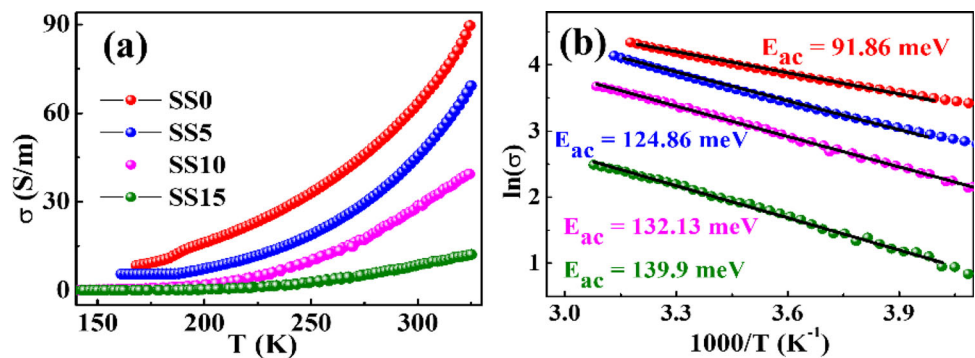


Fig. 2 FESEM images of **a** SS0 (pure SnS) and **b** SS5 (SnS-5%SnO). **c–f** EDAX spectra of SS0-SS15. Inset in **c** is FESEM image of SS0 with point of interest as indicated

Fig. 3 a Temperature dependence of electrical conductivity and **b** $\ln(\sigma)$ versus $1/T$ for $(\text{SnS})_{1-x}(\text{SnO})_x$: $x = 0, 5, 10,$ and 15 nanocomposites



that there are more conductive and less conductive components in the conductivity in the composites; for $x = 0$, it may be due to AB-stacked SnS bilayers with van der Waals forces (Fig. 1e). They have correlation with the change in features of the thermopower discussed below.

In order to know the activation behavior of a typical semiconductor, we fitted the σ data linearly (Fig. 3b) and found that all these samples show the Arrhenius type of behavior in the high-temperature region near 300 K. The σ of $(\text{SnS})_{1-x}(\text{SnO})_x$ NCs follows the relation $\sigma(T) = \sigma_0 \exp[-(E_a/k_B T)]$, where σ_0 , k_B , and T are pre-exponential factor, Boltzmann constant, and absolute temperature, respectively. The activation energies (E_{ac}) calculated from the slope of $\ln(\sigma)$ versus $1/T$ curve of 91.86, 124.86, 132.13, and 139.9 meV for SS0, SS5, SS10, and SS15, respectively

(Fig. 3b and Table S1), are in good agreement with earlier work [60]. It confirms that the transfer of charge carriers from one grain to another is due to the thermal excitation of charge carriers. The activation energy increases with increasing x .

The Seebeck coefficient (α) as a function of temperature drops to a minimum value at 191, 189, 192, and 171 K and increases above these temperatures with increasing temperature in $x = 0, 3.57\%, 7.16\%,$ and 10.79% (Fig. 4a). This trend is in accordance with the electrical conductivity (Fig. 3a). The former features show a dominant resistive component in each in line with those found in the electrical conductivity data below 183, 185, 196, and 200 K (Fig. 3a). The difference in these temperatures in α and σ may be indicative of the slight variation in the responses of these parameters due to the influence of the

dominating surfactants, defects, and grain boundaries over the variation in bond length/angle. In the case of $x = 0$, it is tentatively attributed to AB-stacked SnS bilayers with van der Waals forces (Fig. 1e). The α is 1.53 times larger for SS15 than that of SS0 at 325 K (Fig. 4a and Table S2). The positive values of α for all the samples in the entire temperature range show a p-type conduction in each of them which corresponds to the Sn deficiency (or excess S) shown above (Fig. 2c–f) in line with the literature [14, 40]. The value of α increases with increasing temperature above these characteristic temperatures. It increases with increasing SnO content due to the decrease in the electrical conductivity. Another reason for such a high α is the filtering of charge carriers at the interfaces. Two p-types of semiconductors i.e., SnS and SnO caused this, which increases the average energy per charge carrier [18, 61]. Since SnO at 300 K for nano [39, 40] and bulk [41] has an α of nearly 650 $\mu\text{V}/\text{K}$ and 350 $\mu\text{V}/\text{K}$, respectively, the increase in α with increasing x is attributed to the rising content of SnO in SnS.

Linearly decreasing α with falling temperature reflects the diffusion thermopower. Mott's equation for diffusion thermopower of a nondegenerate p-type semiconductor $\alpha = -\frac{k_B}{e} \left[A + \frac{E_s}{T k_B} \right]$ can be considered, where E_s is the difference between the Fermi level (E_f) to the top of the valence band and A is the constant which depends on the charge carrier scattering [62, 63]. The E_s values determined from the α versus $1/T$ curve fits are 85.9, 106.4, 119, and 134.1 meV for SS0, SS5, SS10, and SS15, respectively (Table S1 and Fig. 4b). It increases as the fraction of SnO content in NCs rises, suggesting that the Fermi level has shifted up (towards the middle of the forbidden band gap),

probably due to the decrease of number of acceptor states.

In order to know the electronic part of the transport properties, the power factor (PF) is studied. This also increases with rising temperature in the entire temperature range (Fig. 4c). It is the maximum for SS5 and the minimum for SS15 (Fig. 4c and Table S2). It is nearly 225 times larger than similar Te-element-free solution-processed and hot-pressed Bi_2S_3 nanorods [64]. It shows the importance of nanostructuring as earlier reports in nanocomposites [6, 7], nanostructures [8, 9], alloy defects [11], liquid phonons [12], and band modification [15–17].

4.1 Thermal conductivity and figure of merit

The total thermal conductivity of SS0, SS5, and SS10 shows a very low value, less than $1.5 \text{ W m}^{-1} \text{ K}^{-1}$, over the entire temperature range studied (Fig. 5a). Its value at 325 K decreases systematically with increasing SnO content due to the strong scattering of phonons at the interfaces in the composites (Table S2; Fig. 5a). κ of SS10 at 325 K is 56% and 84% smaller than those of SS5 and SS0, respectively. The κ obtained for SS10 at 300 K is much smaller than that of SnS previously reported [32, 58, 65–67]. There is a hump each at different temperatures for these samples. The κ drops abruptly below 55 K in SS0. The peak-like feature in κ occurs at around 45 K for SS5. It drops abruptly below this temperature as temperature decreases. It is tentatively attributed to their crystalline nature in the matrix of the NCs. In SS10, the hump has almost disappeared and κ falls linearly below 100 K. As usual, it is assumed for thermal conductivity that its temperature dependence consists of electronic (κ_e) and lattice components (κ_l) i.e.,

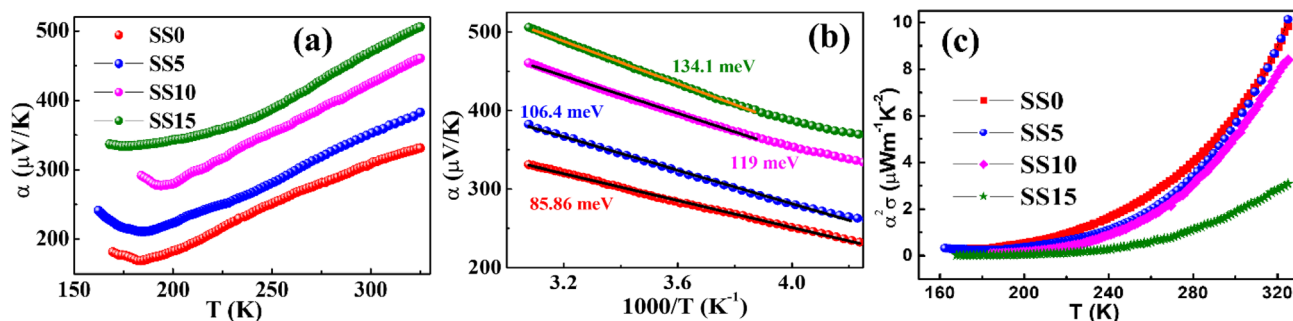


Fig. 4 **a** temperature dependence of Seebeck coefficient (α), **b** α versus $1/T$ curves and **c** thermoelectric power factor for SnS–SnO nanocomposites

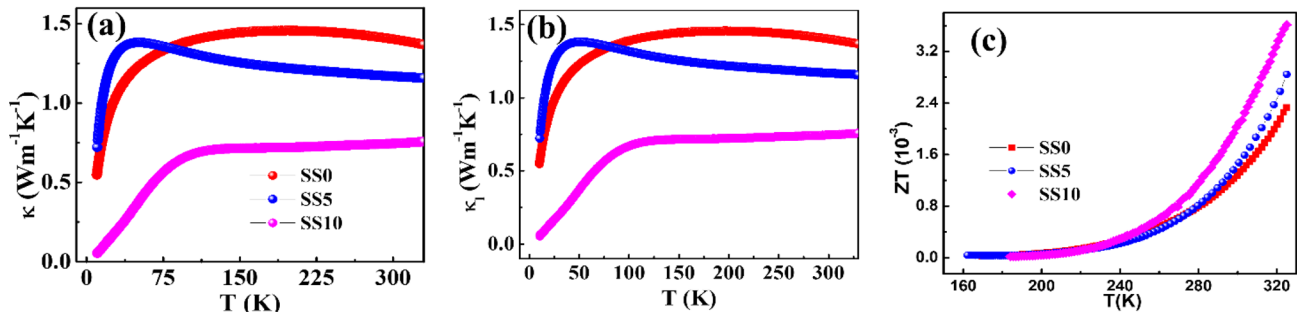


Fig. 5 a Total thermal conductivity, b lattice thermal conductivity, and c figure of merit of SS0, SS10, and SS15

$\kappa = \kappa_l + \kappa_e$. Since σ is related to κ_e through the Wiedemann–Franz law, $\kappa_e = L\sigma T$, where L is the Lorenz number ($2.44 \times 10^{-8} \text{ W}\cdot\Omega \text{ K}^{-2}$); we calculated κ_e for all samples and it is very low because of their poor σ (Figs. 3b and S2). Figure 5b shows the lattice thermal conductivities calculated from $\kappa_l = \kappa - \kappa_e$. They dominate over κ_e , about four orders of magnitude, in the entire temperature range investigated (Figs. 5b and S2). This is interpreted as the importance of nanostructuring/nanocomposite formations. κ_l at 300 K in SS10 is smaller than $\text{Cu}_{1-x}\text{Ag}_x\text{S}$ [61] and SnS [14, 50, 67, 68]. It rises linearly up to 100 K with higher slope, but with gradual decrease of slope making a convex curve and then linearly increasing with very small slope above 120 K as temperature increases. This overall feature is attributed to a large number of point defects. However, it peaks at 45 K, and above this, it decreases as temperature rises due to the probable lower point defects in SS5. It can be clearly seen that κ_l at 300 K decreases with increasing SnS–SnO interfaces in NCs.

The dimensionless figure of merit (ZT) increases with increasing temperature (Fig. 5c). Its value at 325 K of 0.0023, 0.0028, and 0.0036 for SS0, SS5, and SS10, respectively, is poor. It is because of the poor σ . It is 1.55 times larger than that of pure SnS (SS0) at 325 K in SS10 NC. Although it is very low from an application point of view, it has a special importance in connection with TE materials without toxic elements near room temperature. At 325 K, it is $\sim 25\%$ higher than that of other solution-processed nanocomposites without toxic elements such as the Ag inclusion in Ag_2S [18] and Ag-doped CuS [61] at 325 K, but much larger than that of SnO [39]. They agree with the ZT improvement in nanocomposites [6, 7], nanostructures [8, 9], low sound velocity [10], and band modification [15–17] materials. This can be further improved by using proper densification

techniques like hot-press or spark plasma sintering at optimum temperature.

5 Conclusion

We have successfully synthesized NCs of layer-structured $(\text{SnS})_{1-x}(\text{SnO})_x$: $x = 0, 3.57\%, 7.16\%$, and 10.79% using a simple polyol method. The crystallite size of these NCs varies between 25 and 40 nm. The layered orthorhombic crystal structure was derived from the Rietveld refinement of these NCs, which indicates that weak van der Waals interlayer interactions prevail. The FESEM images confirm nanoflake and nanoplate shapes of the SnS NPs. They become thicker with the introduction of SnO and show further growth of SnS nanoflakes with SnO. Such a morphology was confirmed with electrical and thermal transport properties. The positive value of the Seebeck coefficient and the deficiency of Sn in all NPs shows the p-type conduction. The decrease in electrical and thermal conductivities with decreased Seebeck coefficient led to an increase in the dimensionless figure of merit (ZT) with increasing SnO content. ZT maximum at 325 K is 0.0036 and the thermal conductivity at 300 K is $0.75 \text{ Wm}^{-1} \text{ K}^{-1}$ in $(\text{SnS})_{0.928}(\text{SnO})_{0.072}$. The former is 55% improvement compared with pure SnS, and the latter is lower than many other reported tellurium sulfides and selenides. Therefore, this work is very interesting for the future course of research in this direction.

Acknowledgements

Authors gratefully acknowledge Mukul Gupta & Layanta Behera from UGC-DAE Consortium for Scientific Research Indore for XRD data.

Author contributions

CC prepared manuscript and drafting, Tarachand helps in analysis and writing, GSO corrected and helps in analysis of this manuscript, SH measured FESEM and EDAX data, and YKK measured thermal conductivity data.

Funding

UGC-DAE Consortium for Scientific Research, University Campus, Khandwa Road, Indore-452001, India.

Declarations

Conflict of interest There are no conflicts to declare.

Supplementary Information: The online version contains supplementary material available at <http://doi.org/10.1007/s10854-021-05727-7>.

References

- B. Poudel, Q. Hao, Y. Ma, Y. Lan, A. Minnich, B. Yu, X. Yan, D. Wang, A. Muto, D. Vashaee, X. Chen, J. Liu, M.S. Dresselhaus, G. Chen, Z. Ren, *Science* **320**, 634 (2008)
- Y. Lin, C. Norman, D. Srivastava, F. Azough, L. Wang, M. Robbins, K. Simpson, R. Freer, I.A. Kinloch, *ACS Appl. Mater. Interfaces* **7**, 15898 (2015)
- A.T. Duong, V.Q. Nguyen, G. Duvjir, V.T. Duong, S. Kwon, J.Y. Song, J.K. Lee, J.E. Lee, S. Park, T. Min, J. Lee, J. Kim, S. Cho, *Nat. Commun.* **7**, 13713 (2016)
- Z. Deng, D. Han, Y. Liu, *Nanoscale* **3**, 4346 (2011)
- L.D. Zhao, J. He, C.I. Wu, T.P. Hogan, X. Zhou, C. Uher, V.P. Dravid, M.G. Kanatzidis, *J. Am. Chem. Soc.* **134**, 7902 (2012)
- N. Van Nong, N. Pryds, S. Linderoth, M. Ohtaki, *Adv. Mater.* **23**, 2484 (2011)
- B. Liu, J. Hu, J. Zhou, R. Yang, *Materials* **10**, 418 (2017)
- R.J. Mehta, Y. Zhang, C. Karthik, B. Singh, R.W. Siegel, T. Borca-Tasciuc, G. Ramanath, *Nat. Mater.* **11**, 233 (2012)
- Q. Wang, G. Chen, D. Chen, R. Jin, *CrystEngComm* **14**, 6962 (2012)
- W. Li, S. Lin, B. Ge, J. Yang, W. Zhang, Y. Pei, *Adv. Sci.* **3**, 1600196 (2016)
- Y. Han, Z. Chen, C. Xin, Y. Pei, M. Zhou, R. Huang, *J. Alloys Compd.* **600**, 91 (2014)
- H. Liu, X. Shi, F. Xu, L. Zhang, W. Zhang, L. Chen, Q. Li, C. Uher, T. Day, G.S. Jeffrey, *Nat. Mater.* **11**, 422 (2012)
- G. Ding, G. Gao, K. Yao, *Sci. Rep.* **5**, 9567 (2015)
- Asfandiyar, Z. Li, F.H. Sun, H. Tang, J.F. Dong, J.F. Li, *J. Alloys Compd.* **745**, 172 (2018)
- T.-R. Wei, G. Tan, X. Zhang, C.-F. Wu, J.-F. Li, V.P. Dravid, G.J. Snyder, M.G. Kanatzidis, *J. Am. Chem. Soc.* **138**, 8875 (2016)
- T. Fu, X. Yue, H. Wu, C. Fu, T. Zhu, X. Liu, L. Hu, P. Ying, J. He, X. Zhao, *J. Mater.* **2**, 141 (2016)
- H. Wang, A.D. LaLonde, Y. Pei, G.J. Snyder, *Adv. Funct. Mater.* **23**, 1586 (2013)
- Tarachand, B. Mukherjee, M. Saxena, Y.K. Kuo, G.S. Okram, S. Dam, S. Hussain, A. Lakhani, U. Deshpande, T. Shripathi, *ACS Appl. Energy Mater.* **2**, 6383 (2019)
- C.-L. Chen, H. Wang, Y.-Y. Chen, T. Day, G.J. Snyder, *J. Mater. Chem. A* **2**, 11171 (2014)
- W. Li, Z. Chen, S. Lin, Y. Chang, B. Ge, Y. Chen, Y. Pei, *J. Mater.* **1**, 307 (2015)
- S. Acharya, J. Pandey, A. Soni, *Appl. Phys. Lett.* **109**, 133904 (2016)
- H. Tang, J. Dong, F. Sun, P. Shang, J. Li, *Sci. China Mater.* **62**, 1005 (2019)
- X. Hu, W. He, D. Wang, B. Yuan, Z. Huang, L.D. Zhao, *Scr. Mater.* **170**, 99 (2019)
- Asfandiyar, T. Wei, Z. Li, F. Sun, Y. Pan, C. Wu, *Sci. Rep.* **7**, 43262 (2017)
- M.N. Tripathi, C.M. Bhandari, *Pramana - J. Phys.* **65**, 469 (2005)
- S.K. Bux, M.T. Yeung, E.S. Toberer, G.J. Snyder, R.B. Kaner, J.P. Fleurial, *J. Mater. Chem.* **21**, 12259 (2011)
- B. Jiang, P. Qiu, H. Chen, Q. Zhang, K. Zhao, D. Ren, X. Shi, L. Chen, *Chem. Commun.* **53**, 11658 (2017)
- H.H. Xie, C. Yu, T.J. Zhu, C.G. Fu, G.J. Snyder, X.B. Zhao, *Appl. Phys. Lett.* **100**, 254104 (2012)
- C. Bera, S. Jacob, I. Opahle, N.S.H. Gunda, R. Chmielowski, G. Dennler, G.K.H. Madsen, *Phys. Chem. Chem. Phys.* **16**, 19894 (2014)
- M. Michalska, M. Andrzejczuk, K. Oberda, *J. Alloys Compd.* **726**, 388 (2017)
- A. Borde, A. Pawbake, P. Sharma, S. Nair, A. Funde, P. Bankar, M. More, S. Jadkar, *Appl. Phys. A* **124**, 133 (2018)
- B. Zhou, S. Li, W. Li, J. Li, X. Zhang, S. Lin, Z. Chen, Y. Pei, *ACS Appl. Mater. Interfaces* **9**, 34033 (2017)
- D. Parker, D.J. Singh, *J. Appl. Phys.* **108**, 083712 (2010)
- Q. Tan, L. Zhao, J. Li, C. Wu, T. Wei, *J. Mater. Chem. A* **2**, 17302 (2014)
- H. Wu, X. Lu, G. Wang, K. Peng, H. Chi, B. Zhang, Y. Chen, C. Li, Y. Yan, L. Guo, C. Uher, X. Zhou, X. Han, *Adv. Energy Mater.* **8**, 1800087 (2018)

36. W. He, D. Wang, J.F. Dong, Y. Qiu, L. Fu, Y. Feng, Y. Hao, G. Wang, J. Wang, C. Liu, J.F. Li, J. He, L.D. Zhao, *J. Mater. Chem. A* **6**, 10048 (2018)
37. K.C. Kim, S.S. Lim, S.H. Lee, J. Hong, D.Y. Cho, A.Y. Mohamed, C.M. Koo, S.H. Baek, J.S. Kim, S.K. Kim, *ACS Nano* **13**, 7146 (2019)
38. P. Jood, R.J. Mehta, Y. Zhang, G. Peleckis, X. Wang, R.W. Siegel, T. Borca-Tasciuc, S.X. Dou, G. Ramanath, *Nano Lett.* **11**, 4337 (2011)
39. S.A. Miller, P. Gorai, U. Aydemir, T.O. Mason, E.S. Toberer, *J. Mater. Chem. C* **5**, 8854 (2017)
40. N. Salah, W.M.A.A. Alshahrie, S.S. Habib, *J. Mater. Sci. Mater. Electron.* **28**, 3598 (2017)
41. S. Kuwahara, S. Tanusilp, Y. Ohishi, H. Muta, S. Yamanaka, K. Kurosaki, *Mater. Trans.* **59**, 1022 (2018)
42. C. Chotia, B. Mukherjee, M. Saxena, V. Sharma, G.S. Okram, *AIP Conf. Proc.* **2220**, 020017 (2020)
43. Tarachand, M. Saxena, B. Mukherjee, G.S. Okram, *Rev. Sci. Instrum.* **90**, 063904 (2019)
44. A. Soni, G.S. Okram, *Rev. Sci. Instrum.* **79**, 125103 (2008)
45. Y.-K. Kuo, B. Ramachandran, C.-S. Lue, *Front. Chem.* **2**, 00106 (2014)
46. J. Köhler, J. Tong, R. Dinnebier, A. Simon, *Zeitschrift Für Anorg. Und Allg Chemie* **638**, 1970 (2012)
47. N.K. Reddy, M. Devika, E.S.R. Gopal, *Crit. Rev. Solid State Mater. Sci.* **40**, 359 (2015)
48. J.M. Skelton, L.A. Burton, S.C. Parker, A. Walsh, A.J. Jackson, F. Oba, *Phys. Chem. Chem. Phys.* **2**, 12452 (2017)
49. Q. Tan, J. Li, *J. Electron. Mater.* **43**, 2435 (2014)
50. C. Wang, Y. Chen, J. Jiang, R. Zhang, Y. Niu, T. Zhou, J. Xia, H. Tian, J. Hu, P. Yang, *RSC Adv.* **7**, 16795 (2017)
51. M. Park, J.S. Choi, L. Yang, H. Lee, *Sci. Rep.* **9**, 19826 (2019)
52. C. Xin, J. Zheng, Y. Su, S. Li, B. Zhang, Y. Feng, F. Pan, *J. Phys. Chem. C* **120**, 22663 (2016)
53. J.R. Brent, D.J. Lewis, T. Lorenz, E.A. Lewis, N. Savjani, S.J. Haigh, G. Seifert, B. Derby, P. O'Brien, *J. Am. Chem. Soc.* **137**, 12689 (2015)
54. Q.H. Wang, K. Kalantar-Zadeh, A. Kis, J.N. Coleman, M.S. Strano, *Nat. Nanotechnol.* **7**, 699 (2012)
55. T. Björkman, A. Gulans, A.V. Krasheninnikov, R.M. Nieminen, *Phys. Rev. Lett.* **108**, 235502 (2012)
56. B.H. Baby, D.B. Mohan, *Sol. Energy* **174**, 373 (2018)
57. Y. Sun, S. Gao, F. Lei, C. Xiao, Y. Xie, *Acc. Chem. Res.* **48**, 3 (2015)
58. H.Q. Yang, X.Y. Wang, H. Wu, B. Zhang, D.D. Xie, Y.J. Chen, X. Lu, X.D. Han, L. Miao, X.Y. Zhou, *J. Mater. Chem. C* **7**, 3351 (2019)
59. J. Vidal, S. Lany, M. D'Avezac, A. Zunger, A. Zakutayev, J. Francis, J. Tate, *Appl. Phys. Lett.* **100**, 032104 (2012)
60. N.K. Reddy, K.T.R. Reddy, *Solid State Electron.* **49**, 902 (2005)
61. Tarachand, S. Hussain, N.P. Lalla, Y.K. Kuo, A. Lakhani, V.G. Sathe, U. Deshpande, G.S. Okram, *Phys. Chem. Chem. Phys.* **20**, 5926 (2018)
62. A. Amara, A. Drici, M. Guerioune, *Phys. Status Solidi Appl. Res.* **195**, 405 (2003)
63. J.H. Bahk, A. Shakouri, *Phys. Rev. B* **93**, 165209 (2016)
64. Tarachand, V. Sharma, R. Bhatt, V. Ganesan, G.S. Okram, *Nano Res.* **9**, 3291 (2016)
65. R. Guo, X. Wang, Y. Kuang, B. Huang, *Phys. Rev. B* **92**, 11502 (2015)
66. J. Tang, Z. Yao, Z. Chen, S. Lin, X. Zhang, F. Xiong, W. Li, Y. Chen, Y. Pei, *Mater. Today Phys.* **9**, 100091 (2019)
67. A. Shafique, Y. Shin, *Sci. Rep.* **7**, 506 (2017)
68. Y. Han, J. Zhao, M. Zhou, X. Jiang, H. Leng, L. Li, *J. Mater. Chem. A* **3**, 4555 (2015)

Publisher's Note Springer Nature remains neutral with regard to jurisdictional claims in published maps and institutional affiliations.